

# High speed trajectory control using an experimental maneuverability model for an insect-scale legged robot

Benjamin Goldberg, Neel Doshi, and Robert J. Wood

**Abstract**—This paper presents an off-board trajectory controller for a range of stride frequencies (2-45 Hz) that enables zero-radius turns and holonomic control on one of the smallest and fastest legged robots, the Harvard Ambulatory MicroRobot (HAMR). An experimental model is used as the basis for control to capture the highly nonlinear response of the robot to input signals. Closed-loop trajectories are performed with an RMS position error at or below 0.3 body lengths (BL) using gaits at speeds up to 6.5 BL/s (29.4 cm/s) for straight-line and sinusoidal trajectories.

## I. INTRODUCTION

Legged insects demonstrate a remarkable ability to maneuver through their environment during rapid running. For example, cockroaches can maneuver over mesh surfaces and along walls at forward speeds exceeding  $50 \text{ cm s}^{-1}$  and with turning rates of two revolutions per second using distributed sensory and mechanical feedback systems ([1], [2]). In addition to low-level mechanical feedback from their musculo-skeletal structures, insects use simple feedforward controllers to change muscle activation patterns and alter gait [3]. Furthermore, reduced-order dynamical models (templates) such as the Lateral Leg Spring (LLS) and Sliding Spring Leg (SSL) models have explored feedforward control strategies for horizontal plane stabilization ([4], [5]).

Inspired by these capabilities, roboticists have developed a number of legged robots (e.g. RHex, MIT Cheetah, RiSE, and OctoRoACH) to accomplish tasks such as running over rough terrain [6], obstacle traversal [7], climbing vertical surfaces [8], and rapid turning and trajectory control [9], [10]. Furthermore, similar tasks have been achieved with small scale legged robots including RoACH, DASH, and HAMR ([11], [12], [13]).

Robots such as RHex and OctoRoACH successfully implement leg phase and differential drive for trajectory control. In this paper, we extend phase-based control to both heading and lateral velocity. The platform used in this paper for maneuverability and control experiments is the Harvard Ambulatory MicroRobot (HAMR - Fig. 1a), a centimeter-scale, quadrupedal microrobot. Despite its small form factor (4.51 cm long and 1.43 g), HAMR has eight independently actuated degrees of freedom (DOFs) and can run at speeds up to  $10.1 \text{ BL s}^{-1}$  [13]. HAMR has two DOFs per leg – a “swing” that moves in the fore-aft direction, and a “lift” that moves both vertically and laterally (described further in Sec.

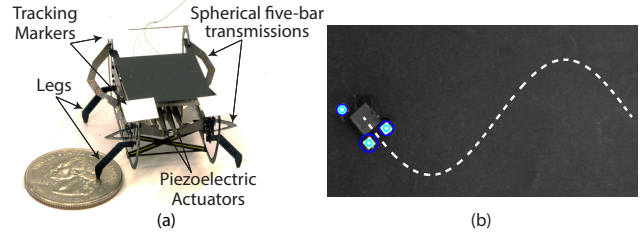


Fig. 1. (a) HAMR-VI, showing the flexure-based transmissions and quadrupedal morphology. (b) Example sinusoidal trajectory that HAMR follows using the off-board, model-based controller.

II). This work leverages all eight DOFs and high bandwidth actuators in HAMR to develop strategies for high speed, controlled running.

In this paper, we show that leg phasing is able to control both heading and lateral position and these maneuvers can be performed across varying stride frequencies and gaits. In Section II and III, we give an overview of HAMR and the maneuverability commands, and in Section IV, we perform open-loop maneuverability experiments. In some regimes, highly nonlinear effects of body dynamics and foot-ground interaction lead to coupling between angular and lateral velocities. Since an analytical model would be prohibitively difficult to develop due to complex system dynamics, experimental data is used to inform controller design for these regimes. Section V describes control experiments with two different gaits at stride frequencies of 2 Hz and 45 Hz. Trajectory following performance is improved with the addition of the experimental maneuverability model that results in an RMS-position error of only 0.07 body lengths (BL). Finally, the controller is evaluated at these low and high stride frequencies by following sinusoidal trajectories and completing an obstacle course.

## II. ROBOT OVERVIEW

Previous versions of HAMR have focused on addressing design and manufacturing limitations to create millimeter-scale mechanisms [14]. This has enabled demonstrations of high speed running and turning [13], climbing [15], and fully autonomous operation with onboard sensing [16]. In these demonstrations, a simple maneuverability scheme was used to control heading and lateral velocity at speeds up to  $0.15 \text{ BL s}^{-1}$  ([16], [17]). Recent redesigns to HAMR’s leg transmissions have increased the leg force output leading to a 114% increase in its payload capacity, and in turn leading to larger step displacements [18]. Additionally, mechanical coupling between contralateral swing DOFs that previously limited gait choice and control options has been removed

The authors are with the John A. Paulson School of Engineering and Applied Sciences, Harvard University, Cambridge, MA 02138, USA, and the Wyss Institute for Biologically Inspired Engineering, Harvard University, Boston, MA, 02115, USA (email: bgoldberg, ndoshi, rjwood@seas.harvard.edu)

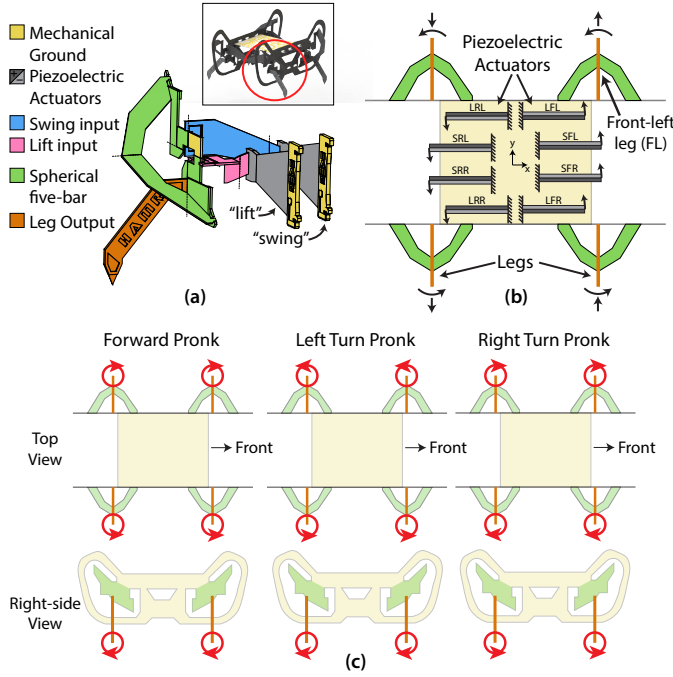


Fig. 2. (a) A perspective view of a single leg transmission and a rendering of the complete robot in the inset. (b) A top view of the robot that shows the the poling of the piezoelectric actuators (dark grey vs. light grey), with a  $180^\circ$  offset between the front and rear actuators. Arrows at the leg and actuator tips indicate motions for a common input signal before the addition of baseline phase offsets to achieve a ‘prong’ gait. (c) Orthogonal top and side views showing the projection of the leg trajectories for turns. For example, during a left turn, the intra-leg phasing for the left legs are reversed by commanding a positive phase offset to the left swing actuators.

and any desired leg phasing can be achieved. These two improvements have led to greater control authority. The following sections give a detailed description of a new maneuverability strategy that uses actuator phasing to control both angular and lateral velocity of HAMR.

#### A. Actuator signal description

There are eight total DOFs in HAMR with two DOFs per leg. Each leg has a ‘swing’ and a ‘lift’ DOF (Fig. 2a and Fig. 3c) that are connected to a single leg output through a flexure-based, spherical five-bar transmission. Each DOF is independently actuated by piezoelectric bimorph actuators with a sinusoidal voltage with three main input parameters as described by the following equation:

$$V_i(t) = \frac{V_b}{2} [1 + \sin(2\pi f_d t + \phi_i)] \quad (1)$$

Here,  $V_i(t)$  is the sinusoidal voltage signal to the  $i^{th}$  actuator as a function of time,  $t$ . The three important parameters are:  $V_b$ , the maximum drive voltage,  $f_d$  the stride frequency, and  $\phi_i$ , the actuator phase.

For actuator phasing, there are two subsets of leg phase variations: *inter-leg* ( $\phi_g$ ) and *intra-leg* ( $\phi_p$ ) phasing. The overall actuator phase is the sum of these two phases ( $\phi_i = \phi_g + \phi_p$ ). While both phases directly affect gait, there are distinct differences between the two. Inter-leg phasing is a global phase variable controlling footfall timings between

each of the individual legs. Intra-leg phasing is a local phase variable between the ‘lift’ and ‘swing’ DOFs that controls the direction and duration of leg footfalls (i.e., swing-stance phase). Intra-leg phase for HAMR is determined by the sum of the last four columns in Table I, choosing left or right turn ( $\phi_p = \phi_b + \phi_{l||r} + \phi_h$ ). The inter-leg and intra-leg phasing is explained in more detail in Section II-B,C, and D.

TABLE I  
ACTUATOR PHASING FOR GAITS AND MANEUVERABILITY

i	DOF*	Gait Offset $\phi_g$	Baseline Offset $\phi_b$	Left Turn $\phi_l$	Right Turn $\phi_r$	Lateral Maneuver $\phi_h$
1	LFL	$\phi_g$	$0^\circ$	0	0	-LP
2	SFL	$\text{FL}_g$	$90^\circ$	+OP	0	0
3	LFR	$\text{FR}_g$	$180^\circ$	0	0	+LP
4	SFR		$270^\circ$	0	+OP	0
5	LRR	$\text{RR}_g$	$0^\circ$	0	0	+LP
6	SRR		$270^\circ$	0	-OP	0
7	LRL	$\text{RL}_g$	$180^\circ$	0	0	-LP
8	SRL		$90^\circ$	-OP	0	0

\*e.g., “LFL”: Lift-front-left, “SRR”: Swing-rear-right  
“OP”: Orientation Phase, “LP”: Lateral Phase

The phase for each DOF is determined by summing all columns of the table (choosing either left or right turn). For heading control, the limits are  $0^\circ \leq \text{OP} < 180^\circ$  and for lateral maneuvers, the limits are  $-60^\circ \leq \text{LP} \leq 60^\circ$  for negative or positive lateral velocities, respectively.

Based on prior successful maneuverability experiments in [13], we decided to focus on actuator phasing to control the robot heading and lateral velocity. Phase is chosen for a number of reasons. First, the basis for standard quadrupedal gaits is leg phasing and therefore phase control is already available and can be used to fine-tune gaits. Furthermore, due to the high voltage requirements of HAMR, phase control is easier to implement than voltage control on future autonomous versions of HAMR. Frequency is another viable option to control heading, however this strategy would preclude turning in place.

#### B. Baseline offset

In order to command standard quadrupedal gaits, mechanical and electrical offsets due to actuator phasing and transmission design need to be taken into consideration. For example, contralateral lift DOFs move in opposite directions (up vs. down) when given the same input signal. These considerations are shown with the arrows in Fig. 2b and they make up the baseline phase offsets in Table I.

#### C. Inter-leg phasing (Gait Offset)

Actuator phasing is the primary method for achieving arbitrary gaits in HAMR. This inter-leg phasing controls the time of footfall for each of the legs with respect to the front-left leg. When  $\phi_g = 0$ , all leg footfalls occur at the same time, commanding the “prong” gait. A schematic of the leg trajectories for the prong are shown in Fig. 2c. Input signals for the prong gait are shown in Fig. 3a with the corresponding expected footfall pattern in (b), and experimental leg trajectories in air tracked in (c). In this paper, two gaits are explored for trajectory control: the trot and jump

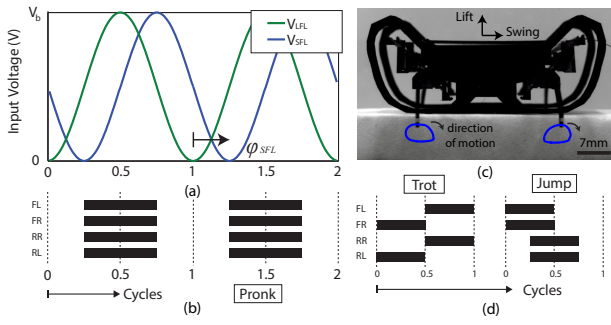


Fig. 3. (a) Example drive signals for the front left leg. The swing DOF input signal ( $V_{SFL}$ ) lags the lift DOF by  $90^\circ$  for nominal circular foot trajectories. For the trajectory control tests in this paper, the bias ( $V_b$ ) voltage is 150 V and the input signal is centered around 75 V. (b) Footfall patterns for the “prong” gait. (c) Foot trajectories from a side-view perspective of the robot suspended on blocks commanding a prong gait. (d) Footfall patterns of the trot and jump gaits.

(footfall patterns shown in Fig. 3d). These gaits are chosen for the ability to achieve high speeds over a range of stride frequencies, however the same maneuverability scheme has been tested and applies to all standard quadrupedal gaits for HAMR (e.g., prong, canter, bound, etc.). It is important to mention that gaits are commanded in the open-loop sense and the timing of actual ground contact may differ from timing prescribed by the input commands.

#### D. Intra-leg phasing

Swing and stance phase is used to control the local, intra-leg phasing,  $\phi_p$ . While changing the intra-leg phasing also affects the observed gait, it does so through variations in the shape of the leg trajectory whereas inter-leg phasing does not modify leg trajectory to alter gait. The last four columns of Table I control the intra-leg phasing with  $\phi_p = \phi_b + \phi_{l||r} + \phi_h$ . The maneuverability scheme for turns and lateral maneuvers are described in the following section.

### III. MANEUVERABILITY SCHEME

The first step to develop a trajectory controller is to design and characterize the performance of an open-loop maneuverability scheme.

#### A. Heading phase command

The basis for heading control for HAMR is differential drive (i.e., “tank steering”) as is common in wheeled robots and some other legged robots (e.g., DASH [12] and OctoRoACH [9]). Leg phase (intra-leg) is used to slow down or reverse the direction of the leg trajectory on the same side of the robot as the desired turn. For a left turn, the intra-leg phasing for the left leg trajectories are reversed by commanding a positive phase offset to the left swing actuators. The opposite is performed for a right turn. These changes in angular velocity are commanded with the phasing modifications shown in Table I (columns five and six). The orientation phase is only added to either the left *or* right side actuators depending on the desired turn direction and is limited to:  $0^\circ \leq OP < 180^\circ$ .

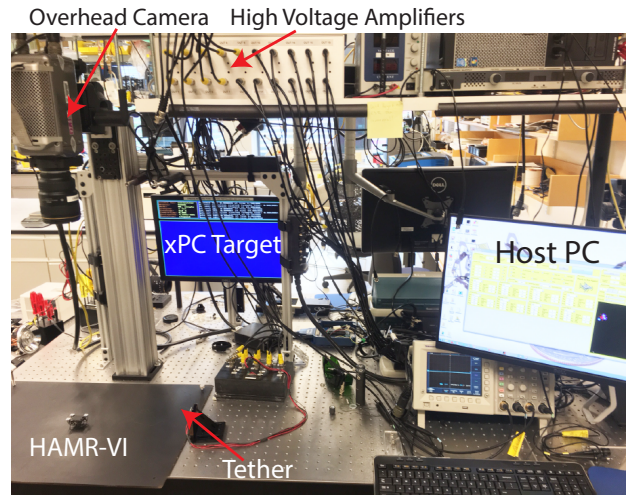


Fig. 4. The experimental setup with the overhead camera. Three white markers are affixed to HAMR for high contrast with the robot chassis and walking surface. The host PC runs the controller and sends control updates to the xPC target that generates waveforms for the actuators that are sent to HAMR through high voltage amplifiers.

#### B. Lateral phase command

Unique to HAMR and other legged systems (e.g., fiddler crabs [19]), the legs can also move in the lateral direction for sideways locomotion. For HAMR, this motion is introduced by a subset of intra-leg phasing shown in column seven of Table I. This input has the effect of swapping the role of the swing and lateral DOFs (i.e. the robot is stepping sideways). The bounds on the lateral phase are limited to  $-60^\circ \leq LP \leq 60^\circ$  to kinematically achieve the maximum lateral velocity.

### IV. FEEDFORWARD MANEUVERABILITY EXPERIMENTS

The maneuverability characteristics for HAMR are experimentally validated by implementing the actuator phasing strategy of Table I. The orientation and lateral phasing is varied from  $-180^\circ$  to  $180^\circ$  and  $-60^\circ$  to  $60^\circ$  with a grid spacing of  $60^\circ$  and  $30^\circ$ , respectively. Seven different gait conditions are tested over this input range – six stride frequencies for the trot gait and one high speed stride frequency for the jump gait. A total of 245 trials are recorded and tracked. The experimental setup to conduct these trials and the results from the feedforward experiments are described in the following sections.

#### A. Experimental setup

The experimental setup consists of two computers in a host/target configuration. The target machine runs Matlab xPC at 5 kHz and receives high level commands (e.g., changes in input actuator phase) from the host machine running Matlab Simulink (Mathworks, r2013b). The low-level drive signal generation is done on the target machine and signals are sent to high-voltage amplifiers (Apex, PA340) through a digital to analog converter installed in the xPC target (United Electronic Industries, PD2-AO-32/16). Amplified voltages are sent through a 10-wire tether (common power and ground plus eight input signals) of 48 AWG wire (MWS wire, 10/48 Unserved Litz). A simple test running



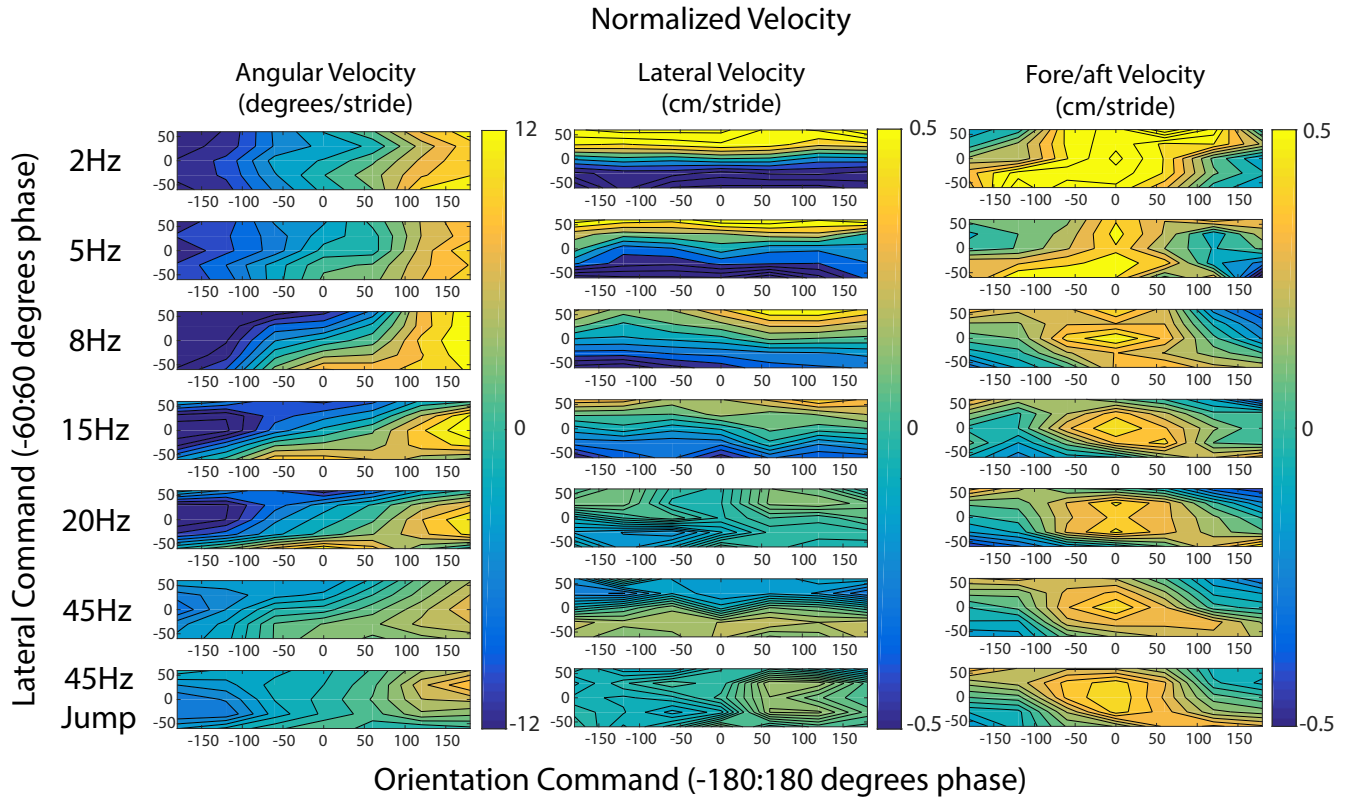


Fig. 5. The results of 245 open-loop maneuverability experiments to control angular and lateral velocities for HAMR. Lateral control authority is decoupled from angular control authority at low speeds (i.e., holonomic motion). Greater amounts of coupling are observed with increases in stride frequency. These experiments are used as a model to inform the trajectory controller.

the robot along different directions of motion relative to the “base” where the tether originates confirms that the tether has negligible mechanical interference on locomotion. As shown in Fig. 4, a high-speed camera (Vision Research, Phantom v7.3) is mounted above the running surface (1/4” acrylic coated in 3M super 77 and matte-black spray-paint for tunable traction) and interfaces to the host computer through ethernet. There are three white tracking markers on HAMR and custom vision processing in MATLAB detects the markers and computes the position and orientation. Feedforward maneuverability experiments are captured by the high speed camera at frame rates up to 675fps for 45 Hz stride frequencies. During closed-loop control experiments, the real-time vision and control runs at an average cycle speed of 30 Hz. Limitations of this feedback rate are described in Sec. VI.

#### B. Angular control authority

Left and right turns are possible at all tested stride frequencies and gaits. The maximum turning rate ranges from 23-407  $^{\circ}/s$  for the 2 Hz trot and 45 Hz jump, respectively. The per-stride angular velocity for each of the input conditions is shown in the left column of contour plots in Fig. 5. Velocities are normalized by the commanded stride frequency for a per-stride measure of velocity. Negative orientation commands produce negative angular velocities, and vice-versa with the exception of conditions where strong coupling effects with lateral commands are observed (discussed in Section

IV-D). On a per-stride basis, angular velocity decreases with increasing stride frequency. We hypothesize this occurs because the legs slip, reducing the effective turning forces. Zero-radius turns, however, are still possible for most gaits. This occurs for input conditions where the lateral velocity and fore/aft velocity are zero (light green in columns two and three of Fig. 5).

#### C. Lateral control authority

Lateral velocities are achieved for a subset of inputs for each tested gait. The magnitude of the maximum lateral velocity ranges from 1.9 to 13.3  $cm\ s^{-1}$  for the 2 Hz trot and the 45 Hz trot, respectively. The per-stride lateral velocity for each of the input conditions is shown in the middle column of contour plots in Fig. 5. For the trot gait at stride frequencies at and below 15 Hz, negative lateral commands produce negative lateral velocities, and vice-versa. Above stride frequencies of 15 Hz, body dynamics and nonlinear effects such as foot-ground interaction begin to change the relationship between control commands and observed lateral velocity. For example, only a combination of orientation phase and lateral phase produce lateral velocities for the 20 Hz trot and 45 Hz jump. In the case of the 45 Hz trot, positive lateral phase commands produce negative lateral velocities, the opposite effect of the lower stride frequency conditions. As stride frequency increases, lateral control authority decreases on a per-stride measure. This is indicated by lighter colors in middle column of Fig. 5 with increasing

stride frequency.

#### D. Angular and lateral coupling

Due to nonlinear effects of body and transmission dynamics and foot-ground interaction at high stride frequencies, there is substantial coupling between angular and lateral velocities at high stride frequencies. At stride frequencies at and below 5 Hz, angular and lateral velocity commands can be considered to be decoupled, as shown in the left and middle columns of Fig. 5. This means that a change in orientation command only produces a change in angular velocity (vertical lines in the first column of Fig. 5). Similarly, a change in lateral command only produces a change in lateral velocity (horizontal lines in the second column of Fig. 5). Above stride frequencies of 5 Hz, there is coupling in the observed angular and lateral velocities for most orientation and lateral commands. If there is no lateral command, however, orientation control is approximately linear with phase.

#### E. Fore/aft velocity

The right column of Fig. 5 shows the normalized fore/aft velocity of HAMR for the given input conditions. Forward velocity generally decreases as phase inputs deviate from the nominal phasing. In extreme cases, there are negative fore/aft velocities (blue regions of third column in Fig. 5). This occurs because the leg trajectories reverse direction and/or move only in the lateral direction for large input orientation and lateral commands. In a controller, these reverse motions can be incorporated or penalized for purposes of preventing backward motions. For simplicity of the trajectory planning in this paper, rearward motions are penalized and only forward trajectories are considered.

### V. CONTROL EXPERIMENTS

The open-loop maneuverability results from the previous sections are used to develop a controller for trajectory following. The following sections describe the controller architecture and compare the controllers at low and high speeds. This control scheme is motivated by simplicity for future autonomy and overcomes complexities of system dynamics and ground contact.

#### A. Controller architecture

A block diagram of the controller architecture is shown in Fig. 6. Feedback for the controller is provided from the high-speed camera mounted above HAMR as shown in Fig. 4. Each image is processed using custom tracking scripts with the image processing and computer vision toolbox in MATLAB. The image processing for the position and orientation (“pose”), as well as the control input calculations are done on the host computer. Control inputs are then sent to the xPC target machine for low-level signal generation. Control inputs are determined separately for lateral and angular velocities, each with their own gains.

Given the desired state, control inputs are calculated using a proportional controller for both the heading and lateral

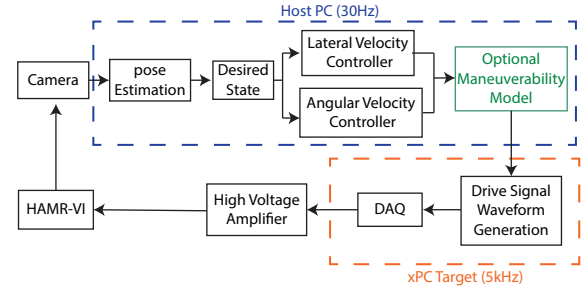


Fig. 6. Architecture of the controller and experimental setup. Phase commands from the lateral and angular velocity controllers can be applied directly to the drive signals or the maneuverability model can be used to determine phasing based on the open-loop maneuverability tests.

position. Integral and derivative gains are omitted due to windup considerations, low feedback rate, and the discrete nature of taking steps which leads to noisy derivatives. The control inputs can either be directly sent as the actuator phasing (no model) for the lateral and orientation command, or the results from the maneuverability experiments can be used as a lookup table (model) to find the commands to achieve the desired angular and lateral velocities.

#### B. Low speed overhead controller

Before more complex trajectories are run, step inputs are commanded to observe the error dynamics. In these tests, the robot starts at a position and orientation with non-zero lateral and heading errors ( $e_{lat} = 6.0\text{ cm}$  and  $e_{\theta} = 30^\circ$ ). The performance for the controller without (Fig. 7a, c) and with (Fig. 7b, d) the model are compared for the 2 Hz trot. At low speeds, the performance with and without the model is similar. In steady-state\*, the RMS errors are 0.3 BL and 0.4 BL for position and  $1.6^\circ$  and  $4.5^\circ$  for orientation with and

\*Steady-state is considered to be when the robot is within  $\pm 0.5$  body widths away from the trajectory and has a heading error within  $\pm 10^\circ$ .

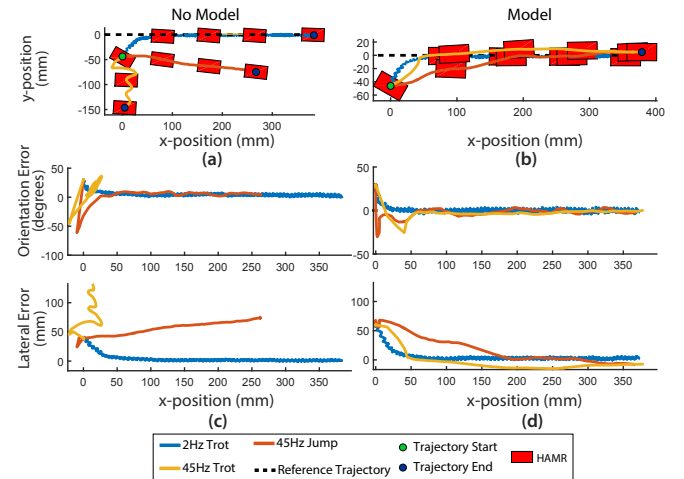


Fig. 7. Step input for low frequency and high frequency gaits for the controller with and without a maneuverability model. The controller fails for high frequency gaits without a model. The robot converges to the reference trajectory with the model, but does so in a longer distance for the 45 Hz gaits compared to the 2 Hz trot gait with and without a model.

TABLE II  
SUMMARY OF PERFORMANCE FOR CONTROL TRAJECTORIES

Gait	Trajectory	Avg. speed (cm/s)	Model (Y/N?)	RMS Position error cm (BL)	RMS Orientation error degrees
2Hz Trot	Sine	1.0	N	0.3 (.07)	11.3*
2Hz Trot	Sine	1.0	Y	0.3 (.07)	7.8*
2Hz Trot	Square	1.2	Y	0.5 (.11)	N/A†
2Hz Trot	Holonomic Sine	1.2	Y	0.6 (.13)	1.5
2Hz Trot	Straight line	1.7	Y	0.3 (.07)	1.6
2Hz Trot	Straight line	1.8	N	0.4 (.09)	4.5
45Hz Trot	Holonomic Sine	10.4	Y	0.9 (.20)	16
45Hz Jump	Straight line	21.2	Y	0.3 (.07)	2.1
45Hz Trot	Straight line	29.4	Y	1 (.22)	3.2

\*Relatively high RMS error due to constantly changing setpoint.

† Steady state error during the straight sections is  $4.2^\circ$ .

without the model, respectively. The robot quickly converges to the desired steady-state within 2.7 cm (0.6 BL). The gains for the angular and lateral controllers are manually tuned to  $k_{p,or} = 6$  and  $k_{p,lat} = 0.4$ . The average speed for the 2 Hz trot is  $1.3 \text{ cm s}^{-1}$  ( $0.29 \text{ BL s}^{-1}$ ). Small oscillations throughout the trajectory occur due to small changes in pose from the stepping motion of HAMR.

After tuning straight-line walking, sine-wave trajectory following is tested. The results of these tests are shown in Fig. 8 and Table II. The RMS-position error for the controller without and with the model is 0.3 cm in both cases. For low speed trajectory-following, the model-based controller has a lower RMS orientation error, but overall there is not a substantial difference between control with and without a model. Compared with previous studies in [17] where the minimum radius of curvature for the trajectory was 15.0 cm, HAMR is now able to successfully follow sinusoidal trajectories with a radius of curvature of 3.3 cm (shown in Fig. 8a). Furthermore, zero-radius turns are now possible with the new turning scheme presented in this paper. This capability is shown in Fig. 8b with a square wave trajectory. Despite the right angle turns, the RMS distance error is 0.5 cm. Finally, holonomic control is shown at low stride frequencies by following a sine-wave trajectory and keeping orientation fixed at  $0^\circ$  (Fig. 8c,d). Position error is 0.6 cm and orientation error is  $1.5^\circ$  for the 2Hz, holonomic trajectory with a radius of curvature of 10.0 cm.

### C. High speed overhead controller

The results of the maneuverability studies in Section IV indicate that angular velocity and lateral velocity become coupled as stride frequency increases and gait is changed. Additionally, in the case of the 45 Hz trot, a positive lateral command results in negative lateral velocity which is the opposite of what occurs in low frequency gaits. These regimes are where a lookup table can substantially improve trajectory following capabilities.

Step inputs are run for two gaits: the 45 Hz jump and trot. Without an experimentally-derived maneuverability mode (subsequently referred to as a “model-based” controller), the same control strategy that works at low stride frequencies results in the robot diverging from the desired trajectory (Fig. 7a). With the model-based controller, however, Fig. 7b shows

that both the high speed gaits are able to control heading and lateral position on the step input trajectories. The RMS position error with the model during steady-state is 0.3 cm for the 45 Hz jump and 1.0 cm for the 45 Hz trot. The larger error for the 45 Hz trot is attributed to the higher overall average speed. The average speed is  $21.2 \text{ cm s}^{-1}$  ( $4.7 \text{ BL s}^{-1}$ ) for the 45 Hz jump and  $29.4 \text{ cm s}^{-1}$  ( $6.5 \text{ BL s}^{-1}$ ) for the 45 Hz trot.

The faster gaits converge over a larger distance than the slower gaits due to the decreased lateral control authority as

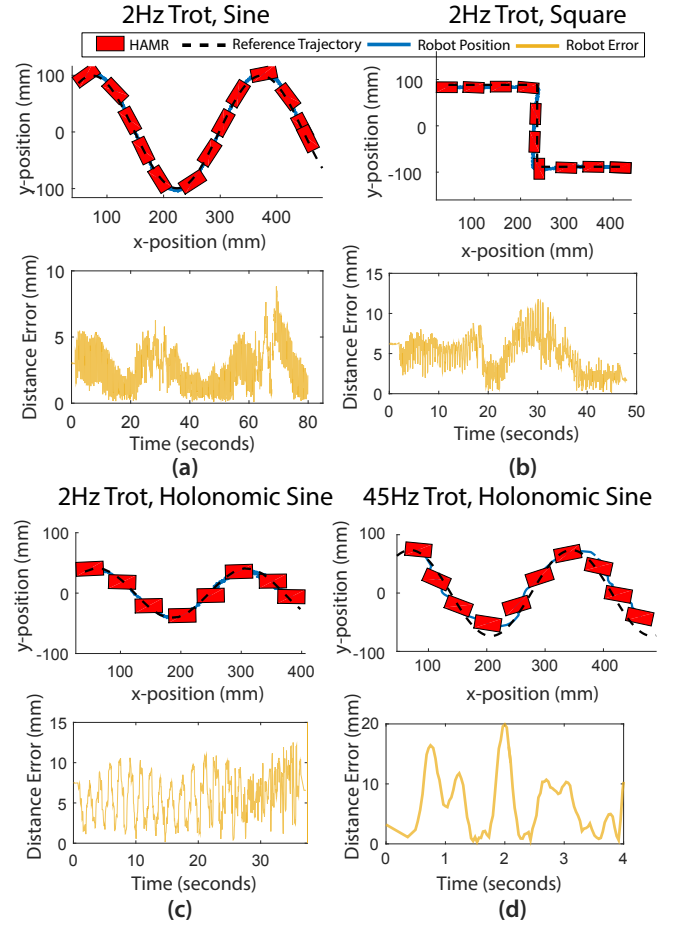


Fig. 8. Trajectory following and control error for four different scenarios: (a) sinusoidal, 2Hz Trot, (b) square wave, 2Hz Trot, (c) holonomic sinusoidal, 2 Hz Trot, (d) holonomic sinusoidal, 45 Hz Trot.

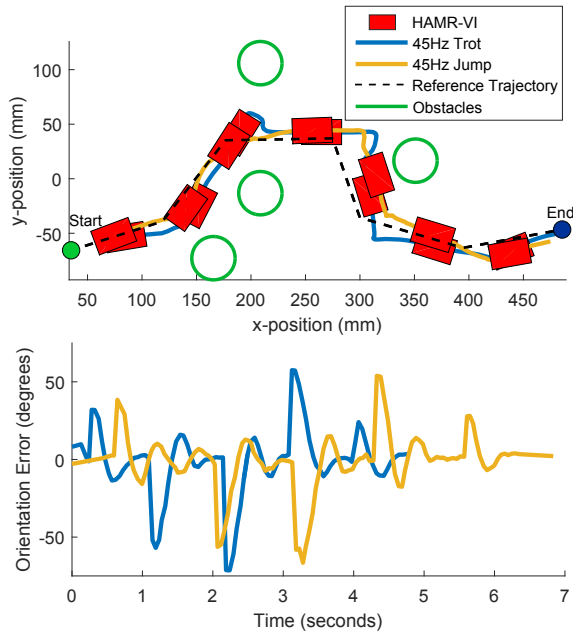


Fig. 9. HAMR navigates through an obstacle course using a model-based controller for high speed gaits. Despite high speed gaits and rapid changes in the commanded position and orientation, the robot is still able to successfully navigate the obstacle course.

mentioned in Sec. IV. The gait that takes the longest distance to converge is the 45 Hz trot which takes 17.1 cm (3.8 BL) to reach steady-state. For comparison, it takes only 2.7 cm (0.6 BL) to reach steady-state for the 2 Hz trot. Despite the longer convergence distance, we are able to perform holonomic control with up to 0.9 cm (0.2 BL) accuracy as shown in Fig. 8d and Table II at a speed of  $10.4 \text{ cm s}^{-1}$  ( $2.3 \text{ BL s}^{-1}$ ).

#### D. High speed obstacle course

After characterizing the step input dynamics for the high speed controller, the robot is run through an obstacle course to demonstrate high speed trajectory following using the model-based controller. The obstacle course is shown in Fig. 9. A trajectory is planned using a gradient descent algorithm and HAMR is able to successfully navigate with both the 45 Hz trot and jump using the model-based controller as shown in the accompanying supplemental video.

## VI. DISCUSSION

Due to highly nonlinear effects of body dynamics and foot-ground interaction of the robot, angular and lateral control differs based on the commanded gait. As the gait is changed (e.g., increasing stride frequency or changing from a trot to a jump) the nature of the coupling between angular and lateral velocities changes in both the magnitude and shape. Additionally, the lateral control authority decreases with increasing stride frequency. It is hypothesized that this is due to effects of body dynamics and foot-ground interactions (e.g., slipping). To capture these effects, an experimental

maneuverability model is found to be useful to map the input leg phasing to output body velocities.

Accuracy of trajectory control at high frequencies is affected by the relatively low feedback rate (30 Hz) compared to low frequencies (1.5 commands per cycle vs. 15 commands per cycle). The relatively low feedback rate is a limitation of the camera and vision processing. With the addition of onboard sensing as demonstrated in [16], higher feedback rates of 100 Hz with sensors such as the ADNS-3530 optical mouse sensor can improve the performance of the high speed trajectory controller. The controller also benefits from being easy to implement onboard an autonomous version of HAMR with actuator phase easily controlled by a microcontroller clock.

## VII. CONCLUSIONS AND FUTURE WORK

A maneuverability strategy based on leg swing-stance phasing is presented and applied to a trajectory controller for low and high speed running for HAMR-VI. Feedback control for lateral and angular position is achieved at speeds ranging from  $1.0$  to  $23.3 \text{ cm s}^{-1}$  ( $0.22$ - $6.5 \text{ BL s}^{-1}$ ). In addition to improving the turning radius of HAMR from 15 cm to a zero-radius turn at low stride frequencies, we also demonstrate a significant increase in average speed during trajectory control on HAMR from  $0.68 \text{ cm s}^{-1}$  to  $29.4 \text{ cm s}^{-1}$ , more than 30 times faster compared to prior work ([16], [17]). Furthermore, we perform aggressive holonomic trajectory following and through an obstacle course in a which was not possible due to the limited control authority of the prior robot and controller designs.

This controller will be applied to future autonomous versions of HAMR that have onboard power and control electronics. Previous versions of HAMR in [16] used a MEMS gyroscope and optical mouse sensor to control position and orientation. Brühwiler et al. implemented a simple orientation controller but the robot had a limited turning radius, stride frequency, gait choice, and no lateral control authority. With the addition of the model-based controller presented here, more complex trajectories can be followed more accurately.

Presumably, complex or textured terrains will have an effect on the performance of the trajectory controller. Future studies should examine these effects and improve foot-ground interactions to achieve faster lateral and turning speeds, especially at high stride frequencies. The benefit of incorporating the experimental model described in this paper is that a simple calibration run can eliminate the need for complex modeling of terramechanics when moving to control experiments on different terrains. In addition to tracking kinematics, force measurements during heading and lateral maneuvers can help determine foot designs that are suitable for reducing slippage and achieving faster turns. Additionally, the controller can be improved by applying other controller architectures such as LQR optimal control by fitting a dynamic model to the experimental data.

Beyond HAMR, using leg phasing for holonomic trajectory control can be extended to other legged robots.

Specifically, robots like OctoRoACH or DASH [9], [12] that have a lateral DOF can apply a similar, phase-based holo-nomic controller. Furthermore, we show that an experimental characterization can be valuable for informing a controller to improve trajectory following performance over a range of stride frequencies.

#### ACKNOWLEDGMENTS

Thank you to all members of the Harvard Microrobotics Lab for invaluable discussions. This work is funded by the Wyss Institute for Biologically Inspired Engineering and the National Science Foundation under Grant Number DGE1144152. Any opinion, findings, and conclusions or recommendations expressed in this material are those of the authors and do not necessarily reflect the views of the National Science Foundation. In addition, the prototypes were enabled by equipment supported by the ARO DURIP program (award #W911NF-13-1-0311).

#### REFERENCES

- [1] J. C. Spagna, D. I. Goldman, P.-C. Lin, D. E. Koditschek, and R. J. Full, "Distributed mechanical feedback in arthropods and robots simplifies control of rapid running on challenging terrain," *Bioinspiration & biomimetics*, vol. 2, no. 1, p. 9, 2007.
- [2] J. Camhi and E. Johnson, "High-frequency steering maneuvers mediated by tactile cues: antennal wall-following in the cockroach," *Journal of Experimental Biology*, vol. 202, no. 5, pp. 631–643, 1999.
- [3] S. Sponberg and R. Full, "Neuromechanical response of musculo-skeletal structures in cockroaches during rapid running on rough terrain," *Journal of Experimental Biology*, vol. 211, no. 3, pp. 433–446, 2008.
- [4] J. Schmitt, M. Garcia, R. Razo, P. Holmes, and R. J. Full, "Dynamics and stability of legged locomotion in the horizontal plane: a test case using insects," *Biological cybernetics*, vol. 86, no. 5, pp. 343–353, 2002.
- [5] D. Zarrouk, A. Pullin, N. Kohut, and R. Fearing, "Locomotion of in-plane robot with continuously sliding feet," in *Proc. CLAWAR*, 2014.
- [6] U. Saranlı, M. Buehler, and D. E. Koditschek, "RHex: A simple and highly mobile hexapod robot," *The International Journal of Robotics Research*, vol. 20, no. 7, pp. 616–631, 2001.
- [7] H.-W. Park, P. M. Wensing, and S. Kim, "Online planning for autonomous running jumps over obstacles in high-speed quadrupeds," in *2015 Robotics Science and Systems Conference, Sapienza University of Rome*, July 13–17, 2015, pp. 1–9.
- [8] M. Spenko, G. Haynes, J. Saunders, M. Cutkosky, A. Rizzi, R. Full, and D. Koditschek, "Biologically inspired climbing with a hexapedal robot," *J. of Field Robotics*, vol. 25, no. 4–5, pp. 223–242, 2008.
- [9] A. O. Pullin, N. J. Kohut, D. Zarrouk, and R. S. Fearing, "Dynamic turning of 13 cm robot comparing tail and differential drive," in *IEEE Intl. Conf. on Robotics and Automation*. IEEE, 2012, pp. 5086–5093.
- [10] K. Karydis, Y. Liu, I. Poulakakis, and H. G. Tanner, "Navigation of miniature legged robots using a new template," in *Control and Automation (MED), 2015 23th Mediterranean Conference on*. IEEE, 2015, pp. 1112–1117.
- [11] A. M. Hoover, E. Steltz, and R. S. Fearing, "RoACH: An autonomous 2.4g crawling hexapod robot," in *IEEE/RSJ Intl. Conf. on Intelligent Robots and Systems*, 2008, pp. 22–26.
- [12] P. Birkmeyer, K. Peterson, and R. S. Fearing, "DASH: A dynamic 16g hexapedal robot," in *IEEE/RSJ Intl. Conf. on Intelligent Robots and Systems*. IEEE, 2009, pp. 2683–2689.
- [13] A. T. Baisch, O. Ozcan, B. Goldberg, D. Ithier, and R. J. Wood, "High speed locomotion for a quadrupedal microrobot," *The International Journal of Robotics Research*, p. 0278364914521473, 2014.
- [14] A. T. Baisch and R. J. Wood, "Pop-up assembly of a quadrupedal ambulatory microrobot," in *Intelligent Robots and Systems (IROS), 2013 IEEE/RSJ International Conference on*. IEEE, 2013, pp. 1518–1524.
- [15] B. F. Seitz, B. Goldberg, N. Doshi, O. Ozcan, D. L. Christensen, E. W. Hawkes, M. R. Cutkosky, and R. J. Wood, "Bio-inspired mechanisms for inclined locomotion in a legged insect-scale robot," in *Robotics and Biomimetics (ROBIO), 2014 IEEE International Conference on*. IEEE, 2014, pp. 791–796.
- [16] R. Bruhwiler, B. Goldberg, N. Doshi, O. Ozcan, N. Jafferis, M. Karpelson, and R. J. Wood, "Feedback control of a legged microrobot with on-board sensing," in *Intelligent Robots and Systems (IROS), 2015 IEEE/RSJ International Conference on*. IEEE, 2015, pp. 5727–5733.
- [17] O. Ozcan, A. T. Baisch, and R. J. Wood, "Design and feedback control of a biologically-inspired miniature quadruped," in *2013 IEEE/RSJ International Conference on Intelligent Robots and Systems*. IEEE, 2013, pp. 1438–1444.
- [18] N. Doshi, B. Goldberg, R. Sahai, N. Jafferis, D. Aukes, and R. J. Wood, "Model driven design for flexure-based microrobots," in *Intelligent Robots and Systems (IROS), 2015 IEEE/RSJ International Conference on*. IEEE, 2015, pp. 4119–4126.
- [19] R. J. Full and C. F. Herreid, "Fiddler crab exercise: the energetic cost of running sideways," *J. exp. Biol.*, vol. 109, pp. 141–161, 1984.